Geochemistry Geophysics Geosystems G3

Article
Volume 00, Number 00
0 MONTH 2013
doi: 10.1002/ggge.20204
ISSN: 1525-2027

Published by AGU and the Geochemical Society

Investigating seismic anisotropy beneath the Reykjanes Ridge using models of mantle flow, crystallographic evolution, and surface wave propagation

A. Gallego, G. Ito, and R. A. Dunn

Department of Geology and Geophysics, School of Ocean and Earth Science and Technology, University of Hawaii, Honolulu HI 96822, USA (agallego75@gmail.com)

[1] Surface wave studies of the Reykjanes Ridge (RR) and the Iceland hotspot have imaged an unusual and enigmatic pattern of two zones of negative radial anisotropy on each side of the RR. We test previously posed and new hypotheses for the origin of this anisotropy, by considering lattice preferred orientation (LPO) of olivine A-type fabric in simple models with 1-D, layered structures, as well as in 2-D and 3-D geodynamic models with mantle flow and LPO evolution. Synthetic phase velocities of Love and Rayleigh waves traveling parallel to the ridge axis are produced and then inverted to mimic the previous seismic studies. Results of 1-D models show that strong negative radial anisotropy can be produced when olivine *a* axes are preferentially aligned not only vertically but also subhorizontally in the plane of wave propagation. Geodynamic models show that negative anisotropy on the sides of the RR can occur when plate spreading impels a corner flow, and in turn a subvertical alignment of olivine *a* axes, on the sides of the ridge axis. Mantle dehydration must be invoked to form a viscous upper layer that minimizes the disturbance of the corner flow by the Iceland mantle plume. While the results are promising, important discrepancies still exist between the observed seismic structure and the predictions of this model, as well as models of a variety of types of mantle flow associated with plume-ridge interaction. Thus, other factors that influence seismic anisotropy, but not considered in this study, such as power-law rheology, water, melt, or time-dependent mantle flow, are probably important beneath the Reykjanes Ridge.

Components: 10,974 words, 8 figures, 1 tables.

Keywords: Reykjanes Ridge; Iceland hotspot; anisotropy; surface waves; seismic inversion; mantle flow.

Index Terms: 8416 Mid-oceanic ridge processes: Volcanology; 1032 Mid-oceanic ridge processes: Geochemistry; 3614 Mid-oceanic ridge processes: Mineralogy and Petrology; 8162 Rheology: mantle: Tectonophysics; 8121 Dynamics: convection currents, and mantle plumes: Tectonophysics; 8033 Rheology: mantle: Structural Geology; 7230 Seismicity and tectonics: Seismology; 1207 Transient deformation: Geodesy and Gravity; 1217 Time variable gravity: Geodesy and Gravity; 1240 Satellite geodesy: results: Geodesy and Gravity; 1242 Seismic cycle related deformations: Geodesy and Gravity; 1952 Modeling: Informatics; 0545 Modeling: Computational Geophysics.

Received 19 April 2013; **Accepted** 14 June 2013; **Published** 00 Month 2013.

Gallego, A., G. Ito, and R. A. Dunn (2013), Investigating seismic anisotropy beneath the Reykjanes Ridge using models of mantle flow, crystallographic evolution, and surface wave propagation, *Geochem. Geophys. Geosyst.*, *14*, doi:10.1002/ggge.20204.

1. Introduction

[2] Observations of seismic anisotropy in the upper mantle are often attributed to strain-induced lattice prefer orientation (LPO) of olivine that occurs during mantle flow. Two basic forms of seismic anisotropy have been identified. One is azimuthal anisotropy, which is detected by an azimuthal variation in body wave travel times [*Backus*, 1965], surface wave phase velocities [*Smith and Dahlen*, 1973], as well as shear-wave splitting [e.g., *Silver*, 1996]. The other is radial anisotropy, also called transverse isotropy, which is typically detected via a discrepancy between the phase velocities of (horizontally polarized) Love and (vertically polarized) Rayleigh waves relative to an isotropic model [*Anderson*, 1961]. Near mid-ocean ridges, anisotropy detected in the lithosphere and asthenosphere has generally been attributed to a preferred orientation of olivine *a* axes (seismically fast axis) roughly horizontal and parallel to the flow direction [e.g., *Shimamura et al*., 1983; *Nishimura and Forsyth*, 1989; *Blackman et al*., 1993; *Forsyth et al*., 1998; *Wolfe and Solomon*, 1998; *Gaherty and Dunn*, 2007; *Nowacki et al*., 2012]. Nevertheless, anisotropy observations along ridges are generally limited in scope, they seldom measure both azimuthal and radial anisotropy, and the interpretations about mantle flow are nonunique and have seldom been tested quantitatively.

[3] A particular mid-ocean ridge setting, where a variety of seismic studies have examined upper mantle dynamics, is the Iceland hotspot and neighboring Reykjanes Ridge (RR). Seismic tomographic studies [*Tryggvason et al*., 1983; *Wolfe et al*., 1997; *Allen et al*., 2002] have confirmed the presence of a hot mantle plume beneath Iceland. Surface wave studies reveal the presence of anomalously low S-wave velocities (<4.1 km/s) extending ≥300 km (~35 Ma seafloor) to either side of the ridge in the upper ~150 km of the mantle (Figure 1) [*Delorey et al*., 2007], an anomaly that is much slower, and wider than low-velocity zones beneath seafloor of similar ages near other ridges [*Gaherty and Dunn*, 2007; *Conley and Dunn*, 2011]. In addition, surface wave measurements reveal that the difference in speed of horizontally polarized S-waves (*Vsh*) compared to vertically polarized S-waves (*Vsv*) is small to slightly positive ($Vsh - Vsv > 0$) directly beneath the ridge, but is clearly negative ($Vsh - Vsv < 0$) in two, ~100 km wide zones on either side of the ridge (Figure 1) [*Gaherty*, 2001; *Delorey et al*., 2007]. Such a pattern of radial anisotropy has yet to be detected beneath any other ridge system.

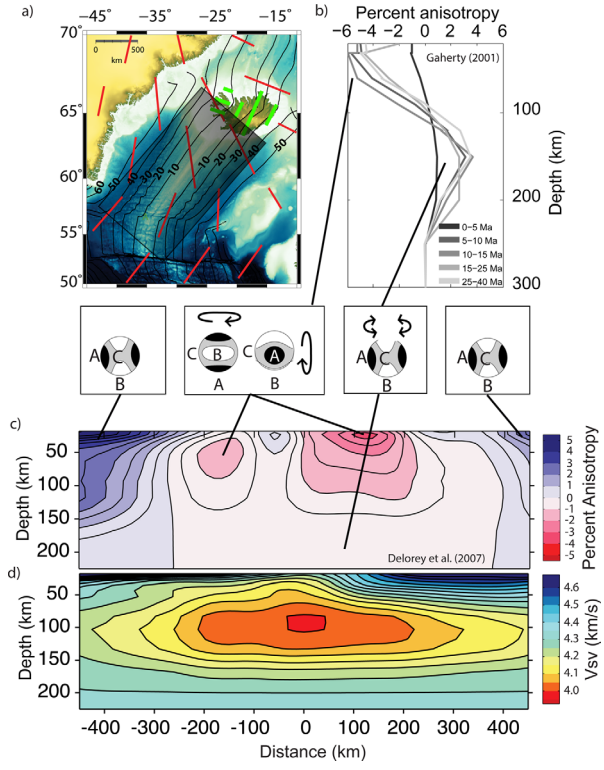

Figure 1. (a) Map of the Reykjanes Ridge and Iceland. The shaded area indicates the approximate region studied by *Gaherty* [2001] and *Delorey et al* [2007]. Red tick marks indicate the orientation of Rayleigh waves azimuthal anisotropy at 75 km depth as determined by *Pilidou et al*. [2005]. Green tick marks indicate azimuthal anisotropy of 50 s Rayleigh waves over Iceland as determined by *Li and Detrick* [2003]. Black lines mark isochrons of the Eurasian and North American plates. (b) Radial anisotropy beneath seafloor of different age ranges from *Gaherty* [2001]. (c) 2-D tomographic solution for radial anisotropy and (d) the corresponding *Vsv* solution of *Delorey et al*. [2007]. In Figures 1b–1d, the seismic models represent the average structure along the Reykjanes Ridge and thus vary only with plate age. Inset diagrams of hemispheres show previous interpretations of the tomography results in Figure 1c; pole figures of V_p for olivine show the orientation of the fast (black), medium (gray), and slow (white) axes.

[4] To explain the off-axis regions of negative radial anisotropy, at least three hypotheses involving mantle plume influence and LPO have been proposed: (1) high mantle buoyancy beneath the ridge, due to melt retention, produces convection cells with a strong upwelling limb beneath the ridge axis and two sinking limbs on the sides of the ridge, where the olivine *a* axes are aligned vertically [*Blackman et al*., 1996; *Gaherty*, 2001]; (2) strong

upwelling beneath the ridge creates a vertical alignment of *a* axes, which is preserved (frozen anisotropy) in the lithosphere as the plates move to the sides of the RR [*Delorey et al*., 2007]; and (3) along-axis plume flow orients the olivine *a* axes along the ridge and creates azimuthal anisotropy such that Rayleigh waves are unusually fast compared to Love waves traveling parallel to the *a* axes, thus giving an apparently high *Vsv* relative to *Vsh* [*Delorey et al*., 2007]. The last hypothesis arises by the fact that the surface waves used in the seismic studies traveled roughly parallel to the Reykjanes Ridge, providing little azimuthal coverage [*Gaherty*, 2001; *Delorey et al*., 2007], therefore prohibiting an independent detection of azimuthal anisotropy. This hypothesis is supported by a local study that shows azimuthal anisotropy with the fast orientation of *Vsv* being roughly parallel to the RR in the shallow upper mantle beneath Iceland [*Li and Detrick*, 2003] and a larger scale study of the whole North Atlantic showing a similar sense of anisotropy over much of the length of the RR [*Pilidou et al*., 2005] (Figure 1a).

[5] Numerical models have been used to explore upper mantle dynamics of plume-ridge interaction [*Ribe et al*., 1995; *Ito et al*., 1996; *Albers and Christensen*, 2001; *Ruedas et al*., 2004] and explain various features of the Iceland hotspot and the RR. In terms of mantle flow structure, two proposed end-member types include a case in which a very low viscosity and thin layer of plume material ponding beneath the lithosphere is strongly channeled along the ridge axis [*Albers and Christensen*, 2001], and the other in which a relatively high viscosity and thick plume layer spreads both along and away from the plume stem in a more radial fashion [*Ribe et al*., 1995; *Ito et al*., 1996, 1999]. The latter situation can occur, for example, as a result of water being extracted from the mantle during partial melting, which should substantially stiffen the mantle above the dry solidus [*Hirth and Kohlstedt*, 1996; *Ito et al*., 1999]. Only recently have these types of flow been tested against observations of shear wave splitting [*Fu et al*., 2012], whereas the effects on surface wave anisotropy have not been studied quantitatively.

[6] The purpose of this study is to investigate the origin of the enigmatic radial anisotropy beneath the Reykjanes Ridge by testing the previous hypotheses and examining different types of flow associated with plume-ridge interaction. Initially, one-dimensional (1-D, depth varying) input models with two imposed anisotropic layers are used to examine the ability of inversions to resolve layered structure and to study the effects of azimuthal anisotropy on inversions for radial anisotropy. Then, we use geodynamic models to simulate mantle flow associated with a mid-ocean ridge (2-D) and plume-ridge interaction (3-D), and compute the development of LPO of an olivine-enstatite assemblage due to that flow. The corresponding seismic anisotropy is used to produce synthetic Love and Rayleigh phase velocities; these synthetic data are inverted for isotropic and anisotropic structure, and then the solutions are compared with those of *Delorey et al*. [2007]. Particular attention is paid to the effects of azimuthal anisotropy on the inversion for radial anisotropy.

2. Methods

2.1. Construction of Anisotropic Elastic Tensors

[7] The temperature-dependent and pressure-dependent elastic tensors were computed from a superposition of an isotropic and an anisotropic part. The isotropic part C_{ij}^{I} was computed based on the method of *Jackson and Faul* [2010]. This method includes the effects of temperature, pressure, grain size, wave period, as well as the anelastic attenuation on shear modulus μ^{F}, based on results of laboratory experiments on olivine aggregates. In the 1-D models, the geotherm used was the solution of a cooling half space plus an adiabatic gradient [*Turcotte and Schubert*, 1982]. In 2-D and 3-D models, temperature was computed numerically (see section 2.2). The resulting shear modulus values and the ratio between the Lamé parameters of PREM [*Dziewonski and Anderson*, 1981] were then used to produce the isotropic part of the elastic tensor, C_{ij}^{I}. For the anisotropic part, we used the code D-Rex [*Kaminski et al*., 2004], which simulates the development of LPO in olivine-enstatite aggregates (section 2.2). From the elastic tensor produced by D-Rex, we extracted the shear modulus μ^{D} and the anisotropic part C_{ij}^{A}. The final elastic tensor was computed from

$$C_{ij} = \frac{\mu^{F}}{\mu^{D}} C_{ij}^{A} + C_{ij}^{I}, \quad (1)$$

where μ^{F} is the shear modulus produced from the *Jackson and Faul* [2010] method, and the ratio μ^{F}/μ^{D} incorporates the temperature and pressure dependence of the anisotropic part of the tensor.

Table 1. Parameters of Mantle Flow Models

	Spreading Rate (km/Myr)	Rayleigh Number	Melt Retention Rayleigh Number[a]	Peak Excess Plume Temperature (°C)	Plume Radius (km)[b]	Viscosity Dependence[c]
Model 1	10	1×10^6	0	N/A	N/A	*T*, *P*
Model 2	10	1×10^6	2×10^7	N/A	N/A	*T*, *P*
Model 3	0	1×10^6	0	200	65 km	*T*, *P*
Model 4	1	6×10^5	0	300	58 km	*T*, *P*
Model 5	10	1×10^6	0	200	65 km	*T*, *P*
Model 6	10	1×10^6	0	200	65 km	*T*, *P*, and water content
Model 7	10	1×10^5	0	300	150 km	*T*, *P*, and water content

[a]Defined by *Ito et al*. [1996].
[b]Radius is distance from the center where excess temperature decays to 1/*e* of the maximum.
[c]Viscosity decreases as an Arrhenius function of temperature *T* and increase exponentially with depth (or, lithostatic pressure, *P*) [*Ballmer et al*., 2007]. In Models 6 and 7, viscosity depends inversely on the content of water dissolved in the solid [*Hirth and Kohlstaedt*, 2003].

2.2. Construction of Anisotropy Structure for 2-D and 3-D Geodynamic Models

[8] Two-dimensional (2-D) geodynamic models of a mid-ocean ridge without a plume, and 3-D models of plume-ridge interaction were produced using the mantle convection code Citcom [*Moresi and Gurnis*, 1996; *Zhong et al*., 2000]. Citcom uses finite elements to solve the equations of mass, momentum, and energy conservation in a convecting, viscous fluid with the extended Boussinesq approximation [*Bianco et al*., 2008]. The Cartesian volume was discretized with 128 × 64 elements in box sizes of 800 × 400 km (values given for *x, z*, respectively) for 2-D models, and 128 × 128 × 64 elements in box sizes of 800 × 800 × 400 km (values given for *x, y, z*, respectively) for 3-D models. Element size was refined near the ridge axis. Temperature at the surface was maintained at 0°C and seafloor spreading was simulated by moving the top boundary. In the 3-D models, a plume stem was imposed with a circular thermal anomaly at the bottom boundary relative to the background potential temperature of 1350°C everywhere else on the model base (see Table 1 for plume temperature and radii). Viscosity decreases as an Arrhenius function of temperature and increases exponentially with depth (or lithostatic pressure). In some models, viscosity also depends inversely on the mantle water content [*Hirth and Kohstedt*, 2003], which creates a viscous layer where the mantle has been dehydrated by partial melting [*Hirth and Kohlstedt*, 1996]. The outputs of CITCOM are the absolute temperatures and the mantle flow velocities.

[9] The mantle flow field was used to compute LPO and seismic anisotropy using the D-Rex algorithm [*Kaminski et al*., 2004]. This approach, for example, has been shown to produce seismic anisotropy parameters (assuming hexagonal symmetry for elastic tensors) in models of global mantle flow that statistically match those of laboratory experiments [*Becker et al*., 2006]. D-Rex simulates the development of LPO due to ductile deformation and dynamic recrystallization of olivine (75%) and enstatite (25%) aggregates along material flow paths. We assumed the A-type of olivine fabric, which is expected in peridotite with low-water content and thought to be the dominant fabric in the upper mantle near mid-ocean ridges [*Karato et al*., 2007]. The D-Rex parameters that control the rate of grain boundary migration and new grain growth were set to $M = 125$ and $\lambda = 5$, respectively [*Kaminski et al*., 2004]. A Voigt average of an assemblage of 1300 crystals yielded the anisotropic elastic tensors throughout the model volume at every other finite element node. The output of D-Rex and the mantle temperature field were then used to calculate the full temperature and pressure-dependent anisotropic elastic tensors as described in section 2.1.

2.3. Synthetic Surface Wave Phase Velocities, Inversions, and Comparison with Input Models

[10] From the model anisotropic elastic structure, we calculated synthetic surface wave phase velocities using the method of *Takeuchi and Saito* [1972]. Since this method does not include the effects of azimuthal anisotropy, we added azimuthal-dependent perturbations to the phase velocities using the formulation of *Montagner and Nataf* [1986] (see supporting information Appendix A1).[1] To mimic the experiment of *Delorey et al*. [2007], we considered the phase velocities of surface waves propagating in a single direction,

[1]Additional supporting information may be found in the online version of this article.

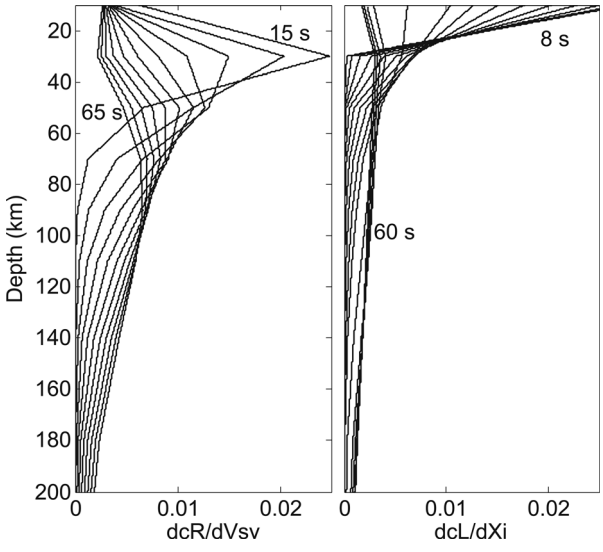

Figure 2. Examples of sensitivity functions calculated in the forward modeling of Love and Rayleigh phase velocity. Each curve represents the partial derivative of (left) Rayleigh and (right) Love waves speeds (*cR* and *cL*, respectively) with respect to *Vsv* and *Vsh/Vsv*, respectively, for each period (ranges labeled and each curve at 65, 60, 55, 50, 45, 40, 35, 30, 25, 20, 15 s for Rayleigh waves, and 60, 50, 40, 30, 20, 17, 16, 15, 14, 13, 12, 11, 10, 9, 8 s for Love waves). Curves are for the 1-D models but look similar in the 2-D and 3-D geodynamic models.

parallel to the ridge axis. For 1-D models, one set of phase velocities for a range of Love and Rayleigh wave periods was produced. For 2-D models, the sets of phase velocities varied laterally across the model (perpendicular to the ridge axis). For 3-D models, maps of synthetic surface wave phase velocity for each period were calculated and then time averaged in the direction parallel to the ridge, thereby producing average phase velocities of surface waves propagating parallel to the ridge as a function of distance normal to the ridge—a situation much like the original seismic experiments. We used Rayleigh wave periods of 10–65 s and Love wave periods of 8–60 s, which have depth-varying sensitivities to *Vsv* and *Vsh/Vsv*, respectively, shown in Figure 2.

[11] Similar to *Delorey et al*. [2007], we jointly inverted the Love and Rayleigh phase velocities for *Vp*, *Vsv*, and radial anisotropy, $(Vsh - Vsv)/[(Vsh + Vsv)/2]$, using a least squares iterative method (see supporting information Appendix A2). The variance, correlation length, and depth of grid points were chosen to produce solutions matching the characteristics of the input model. We emphasize that while the synthetic phase velocities include contributions from both radial and azimuthal anisotropy, the inversion solved for radial anisotropy alone, so direct comparisons could be made with the results of *Delorey et al*. [2007].

[12] The last step in the analysis of the models was to compare the solutions of inversions with the same properties of the original input model. Doing so required a direct calculation of *Vsv* and $(Vsh - Vsv)/[(Vsh + Vsv)/2]$ from the input elastic tensors for which we used the formulations of *Montagner and Nataf* [1986] (see supporting information Appendix A3).

3. Results of 1-D Model Calculations

[13] Using 1-D input models with two layers of uniform anisotropy, we investigate the effects of layer thickness and LPO orientation on the solutions of synthetic surface wave inversions. Figure 3 illustrates the properties of the elastic tensor used here; only the orientation of the tensor varies between model layers, not its magnitude. Figure 4 shows the results of varying the thickness of the upper layer and keeping the orientation of the LPO (elastic tensor) the same between different input models. Figure 5 shows the results of varying the LPO (tensor) orientation, but with unchanging layer thickness.

3.1. Ability of Inversions to Resolve Layered Structure

[14] Four separate 1-D velocity models were formed by starting with the 1-D isotropic model described in section 2.1 and adding an upper anisotropic layer with negative anisotropy such that the olivine *a* axes were preferentially aligned vertically, the *b* axes were aligned perpendicular to wave propagation, and the *c* axes were aligned horizontally, parallel to wave propagation. The difference between the four models is only in the thicknesses of the upper layer, which was 50, 100, 150, and 200 km (Figures 4a–4d, respectively). The lower layer (extending to a depth of 400 km) had positive anisotropy, with the *a* axes (Figure 2) aligned horizontally and perpendicular to wave propagation, the *b* axes aligned vertically, and the *c* axes aligned parallel to wave propagation. The negative anisotropy in the top layer leads to slower Love waves and faster Rayleigh waves compared to without anisotropy, and this effect increases with increasing top layer thickness. The inversions successfully recover the negative anisotropy in the top layer in all cases. If the thickness of the top

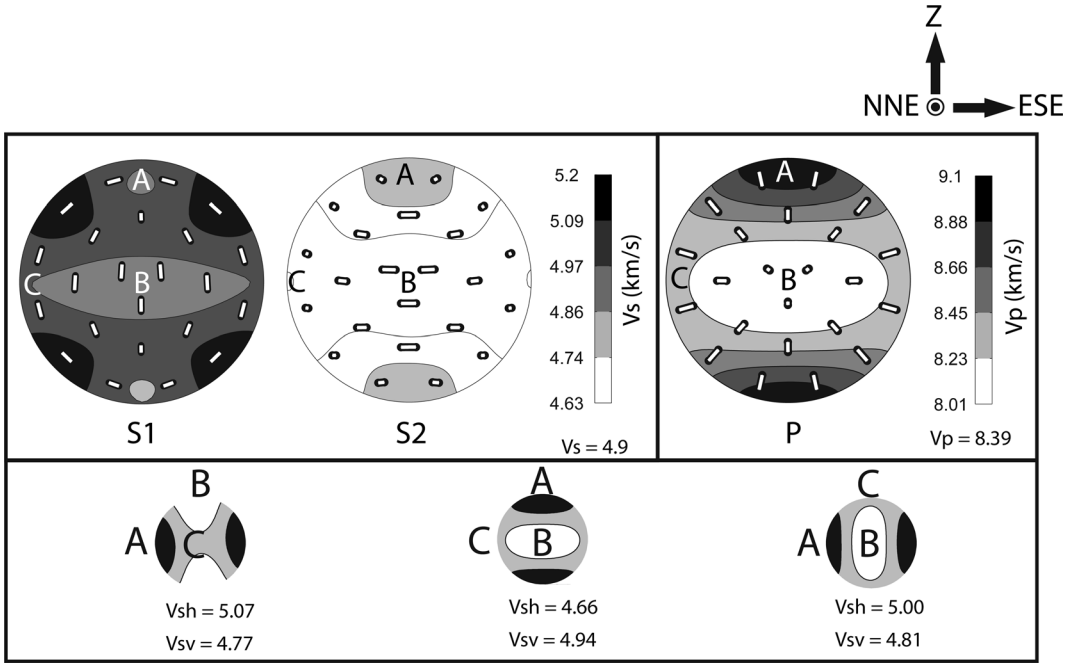

Figure 3. (top row) Pole figures of body wave velocity and polarization for an aggregate of olivine (75%) and enstatite (25%) subject to a constant simple shear with LPO computed using D-Rex [*Kaminski et al.*, 2004]. Velocities are shaded and polarization directions are shown as tick marks. (left) Fast (S1) and slow (S2) shear velocities. (right) *Vp*. The preferred orientation of the olivine axes are marked with their corresponding letters (A [1 0 0], B [0 1 0], and C [0 0 1]). All the calculations in this study are geographically oriented as indicated by large arrows with the vertical axis (Z) up, ESE (ridge perpendicular) right and NNE (ridge parallel) normal and into the shown plane. (bottom) The same crystal aggregate is orientated differently (again labeled with letters) as shown by hemisphere plots of *Vp* with labeled azimuthal average velocities along the equator of the pole figures for shear waves polarized horizontally (*Vsh*), and vertically (*Vsv*).

layer is $\leq\sim$150 km, the inversions also recover the positive anisotropy in the bottom layer as well as the approximate depth at which the anisotropy changes sign. The inversions do not resolve the sharp, step-function shape of the input model but instead predict smoother variations with depth, thus leading to magnitudes of radial anisotropy that overshoot the input model at some depths, and undershoot the input model at other depths. Structure deeper than $\sim$150 km is generally not resolved, primarily because the surface waves of the periods used are relatively insensitive to structure at these depths. Azimuthal anisotropy introduces small, but inconsequential differences in both input model and solutions in these cases.

[15] These results inform us about the ability of the inversions to resolve layered structure in 3-D geodynamic models (section 4) as well as beneath the Reykjanes Ridge. Namely, the inversions are likely to distinguish two layers if the top is thinner than $\sim$150 km, and the solutions are likely to have variations that are as smooth or smoother than the real structure. This exercise further illustrates the confidence in the prior inversions of data from the Reykjanes Ridge in resolving negative anisotropy ($<-0.5\%$) on the sides of the ridge at depths $<$100–150 km [*Gaherty*, 2001; *Delorey et al.*, 2007].

3.2. Effects of Azimuthal Anisotropy on Apparent Radial Anisotropy

[16] The next set of calculations examined differences in the orientation of LPO. In these cases, the top layer had a fixed thickness of 100 km. Again, an input structure with the top layer having a negative anisotropy (*a* axes vertical) leads to slower Love waves and faster Rayleigh waves relative to the isotropic structure. Likewise, positive anisotropy (*a* axes horizontal, at any angle relative to the direction of wave propagation) in the top layer, leads to faster Love and slower Rayleigh waves.

[17] Using synthetic data from the input structure with only radial anisotropy, the inversions generally recover the magnitude and sign of the anisotropy in the top layer as well as the depth of the

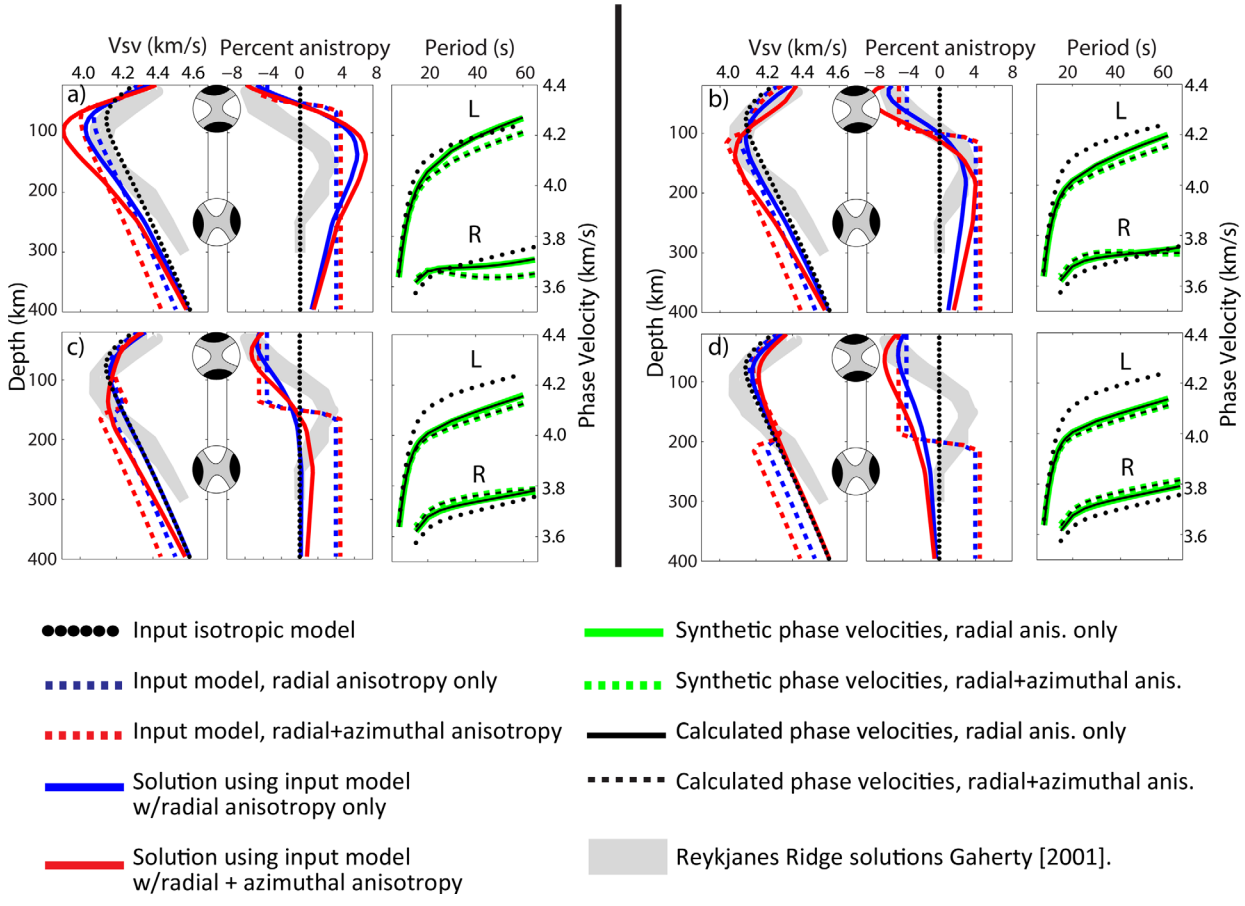

Figure 4. Effects of anisotropic layer thickness on inversions. Thickness of the upper layer are (a) 50 km, (b) 100 km, (c) 150 km, and (d) 200 km. Anisotropy of each layer is the same in all cases and shown with pole plots of *Vp*, and shading encompasses the preferred orientations of the olivine a (fast black) axes, c (intermediate gray) axes, and b (slow white) axes. Each subpart includes (left) vertical shear velocity (*Vsv*), (middle) percentage of apparent anisotropy ($100 \times (Vsh - Vsv)]/[(Vsh + Vsv)/2]$), and (right) phase velocities of Love (L) and Rayleigh (R) waves. Each input model (structural velocities by direct calculation shown by dashed red and blue lines) is used to produce synthetic phase velocities data (green lines), which are used to invert back to body wave structure (continuous red and blue lines) and by fitting the phase velocities (black lines). One set of inversions is based on synthetic phase velocities with radial anisotropy only (blue dashed curves) and, the other set includes radial + azimuthal anisotropy (red dashed) (but again we invert only for radial anisotropy for all cases). The starting point of the iterative inversion method is isotropic (dotted black line). For information only, not direct comparison, the thick gray regions show the range of solutions for the RR over seafloor ages of 5–40 Myr from *Gaherty* [2001].

transition between the top and bottom layers when present. But when the effects of both azimuthal and radial anisotropy are included, the differences between the input model and solutions of the inverse problem are variable. On one hand, when the *a* axes in the top layer are dominantly orthogonal to the direction of wave propagation (either horizontally or vertically oriented), azimuthal anisotropy has a small effect on the apparent radial anisotropy of the input model as well as the solutions (Figures 5a–5d) (again for *S*-waves propagating parallel to the ridge axis). On the other hand, when the *a* axes in the top layer have a large component parallel to the direction of wave propagation, azimuthal anisotropy creates large changes in the apparent radial anisotropy in the input models, and even large differences in the solutions (Figures 5e–5j). For example, when the *a* axes are parallel to wave propagation and the *b* axes are vertical in the top layer (Figures 5e and 5f), azimuthal anisotropy shifts the apparent radial anisotropy of the input model to less positive values (red dashed

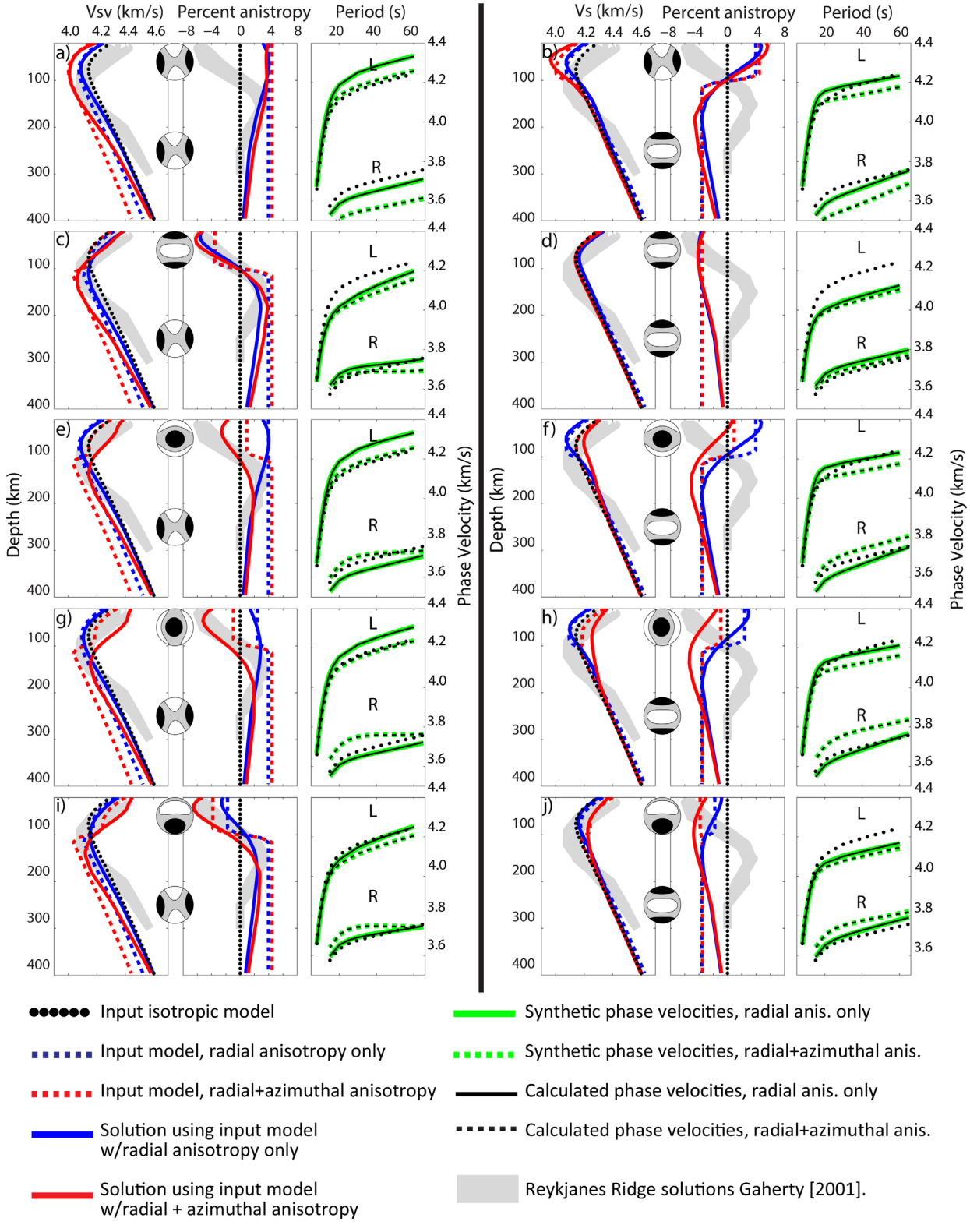

Figure 5. Effects of LPO orientation on phase velocities and inversions for radial anisotropy. Same as Figure 4 but for a constant top layer thickness (100 km) and different orientations of LPO as shown by pole plots. Olivine *a* axes preferentially oriented (left column) horizontally versus (right column) vertically in the lower layer. (a–j) From top to bottom, the orientation of LPO in the upper layer changes; side-by-side parts have the same upper layer orientation.

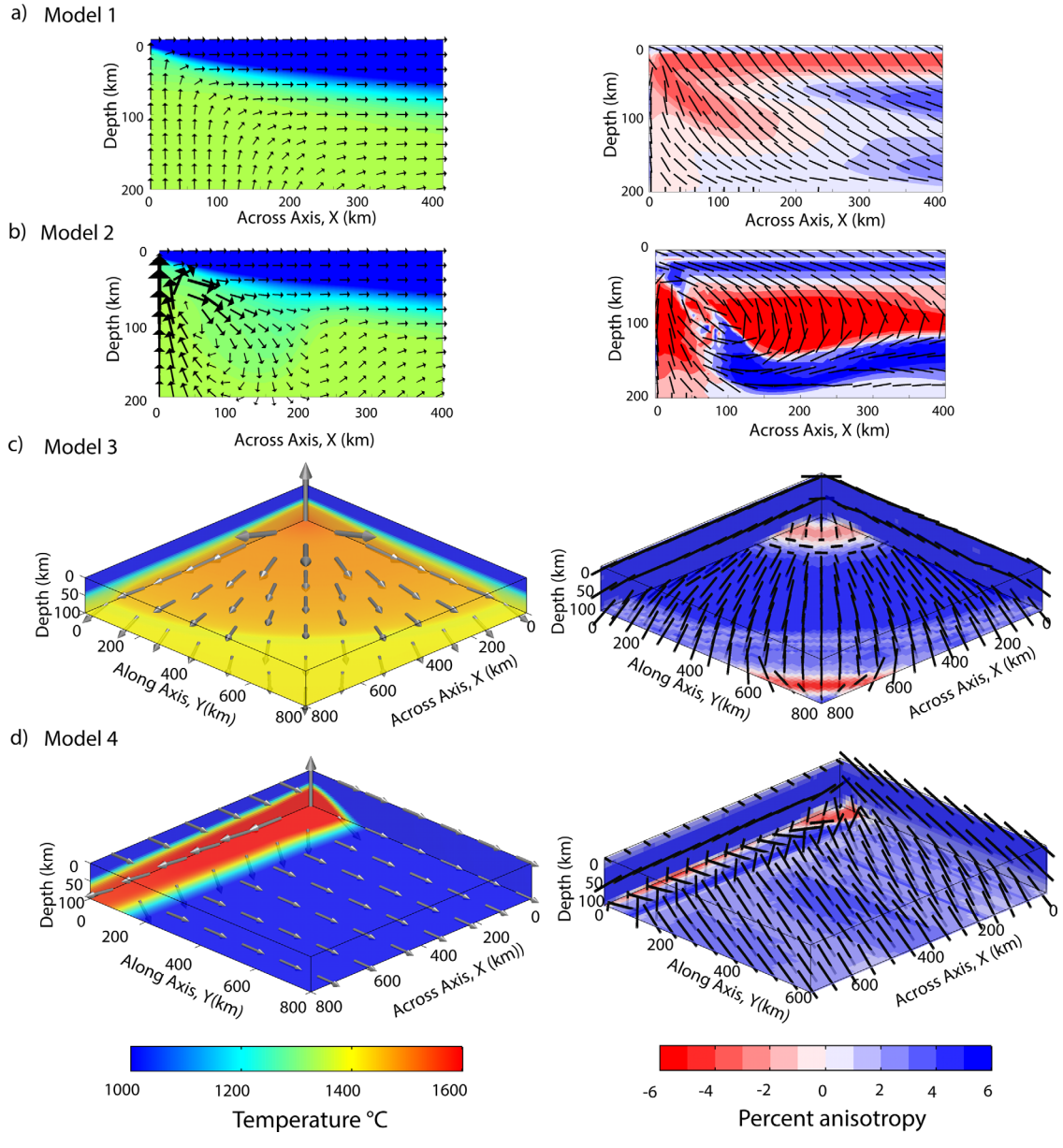

Figure 6. (left column) Mantle flow models show magnitude and direction (arrows) of the mantle flow velocities and potential temperatures (colors). (right column) Seismic anisotropy computed directly from the corresponding geodynamic model show preferred directions of the olivine *a* axes (black bars) and degree of radial anisotropy ($100 \times [Vsh - Vsv]/[(Vsh + Vsv)/2]$) (colors). Models are of (a) 2-D mantle flow, driven passively by seafloor spreading beneath a mid-ocean ridge (half spreading rate is 10 km/Myr); (b) 2-D active mantle flow due to melt-retention buoyancy beneath a mid-ocean ridge (same spreading rate as Figure 6a); (c) 3-D radial spreading of a mantle plume beneath stationary lithosphere (no seafloor spreading); (d) strong channeling of a mantle plume along an ultraslow spreading (1 km/Myr) mid-ocean ridge; (e) a low-viscosity plume interacting with a ridge without the effects of water on rheology; (f) plume interacting with a ridge with a dehydrated and high-viscosity layer in the shallowest upper mantle (plume radius is 65 km and Rayleigh number is 1×10^6); and (g) same as Figure 6f but with a wider plume (150 km radius) and lower Rayleigh number (1×10^5). Half spreading rate is 10 km/Myr in Figures 6e–6g.

curve) as compared to the models with radial anisotropy only (blue dashed curve). Correspondingly, the solutions with the input azimuthal anisotropy (red solid curve) are also shifted to less positive values, but so much so that the solutions actually recover a negative anisotropy in the top layer, not the small positive anisotropy of the input model. When the *a* axes are parallel to wave propagation and the *b* axes are horizontal and perpendicular to wave propagation (rather than vertical as in the former case), azimuthal anisotropy shifts the apparent radial anisotropy to negative values

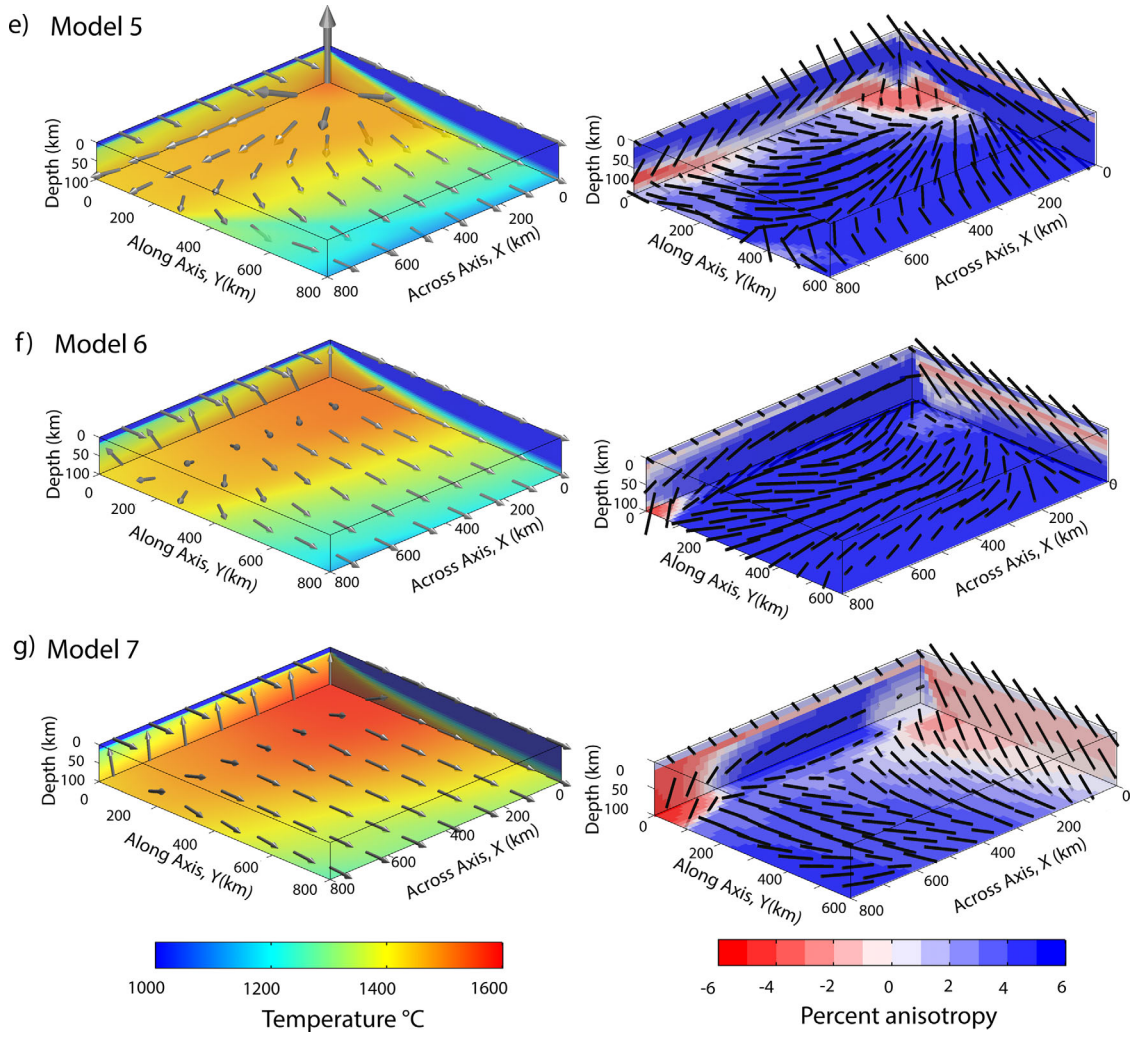

Figure 6. (Continued)

in the input model and even larger negative values in the solutions (Figures 5g and 5h). These effects are maximized when the *a* axes are 45° from vertical in the plane of wave propagation and the *c* axes are horizontal, orthogonal to wave propagation (Figures 5i and 5j). Because the inversions solve for radial anisotropy only, data with inherent azimuthal anisotropy produce a larger trade off between isotropic and radially anisotropic velocity structure, which reduces the uniqueness of the solution. In addition, because the inversion solves a nonlinear problem, the solution is to some degree biased toward the starting, trial solution of the iterative inversion method (see supporting information Appendix 1.1). For real data, such biases can be addressed by examining a range of starting trial solutions. In the current inversions, the starting solution again, comes from the isotropic part of the elastic tensors.

[18] The above results illustrate that when surface waves do not have good azimuthal coverage, azimuthal anisotropy in the mantle can create large effects on the apparent radial anisotropy. Relevant to the prior interpretations of the Reykjanes Ridge tomography, the current results demonstrate that vertically aligned *a* axes, and inferred mantle flow, is but one possible cause for the large negative anisotropy found along this ridge. A full or partial alignment of the *a* axes and mantle flow, parallel to wave propagation can also lead to negative anisotropy comparable in magnitude to that seen near the RR.

4. Results of Geodynamic Model Calculations

[19] Geodynamic models were used to predict mantle flow, track the evolution of LPO as it

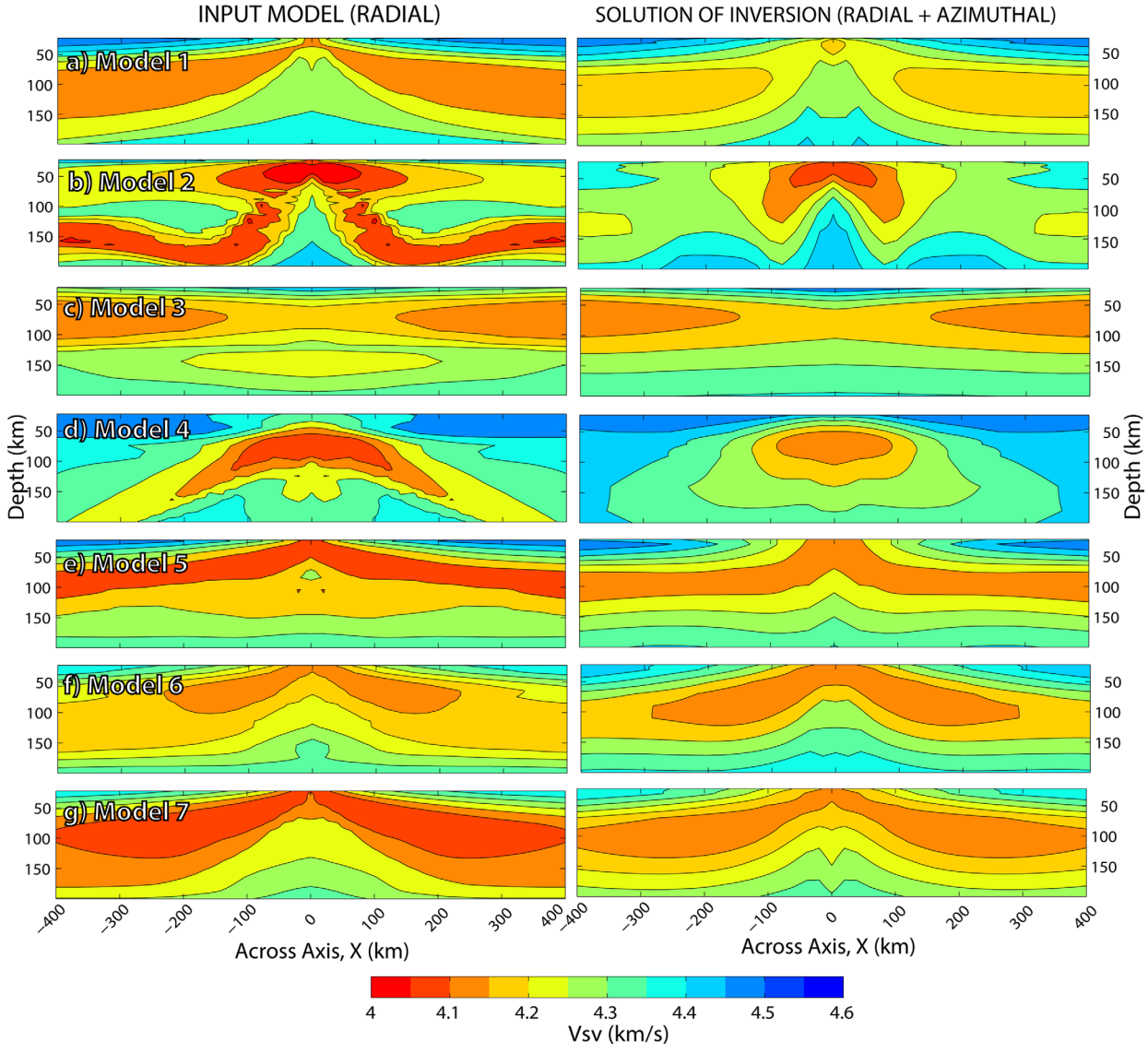

Figure 7. (left column) *Vsv* from the input models in Figure 6, determined by averaging parallel to the ridge axis. (right column) *Vsv* solutions of joint inversion of synthetic Rayleigh and Love wave phase velocities produced from the input models, including the effects of both radial and azimuthal anisotropy. Figures 7a–7g are in the same order as for Figure 6.

develops with the flow, and test previous hypotheses about the origin of seismic anisotropy along the Reykjanes Ridge. Seven models were examined. Models 1 and 2 are idealized cases of a ridge without a plume. The next two models simulate idealized, end member types of plume flow: axisymmetric, radial flow away from the plume stem (Model 3), and nearly unidirectional channeled flow along the ridge axis (Model 4). The last three models are more realistic cases of Icelandic plume-ridge interaction; the first of these considers a low-viscosity plume with a temperature-dependent rheology (Model 5), and the following two include high viscosities in the ponding plume material due to the added effects of water-dependent rheology (Models 6 and 7). The detailed model parameters are given in Table 1. In all cases, the synthetic phase velocities used in the inversions include the effects of both radial and azimuthal anisotropy.

4.1. Models 1 and 2: 2-D Mantle Flow Beneath a Mid-Ocean Ridge Without a Plume

[20] Model 1 simulates 2-D mantle flow that is driven passively by seafloor spreading. In this case, mantle rises beneath the ridge, turns a corner,

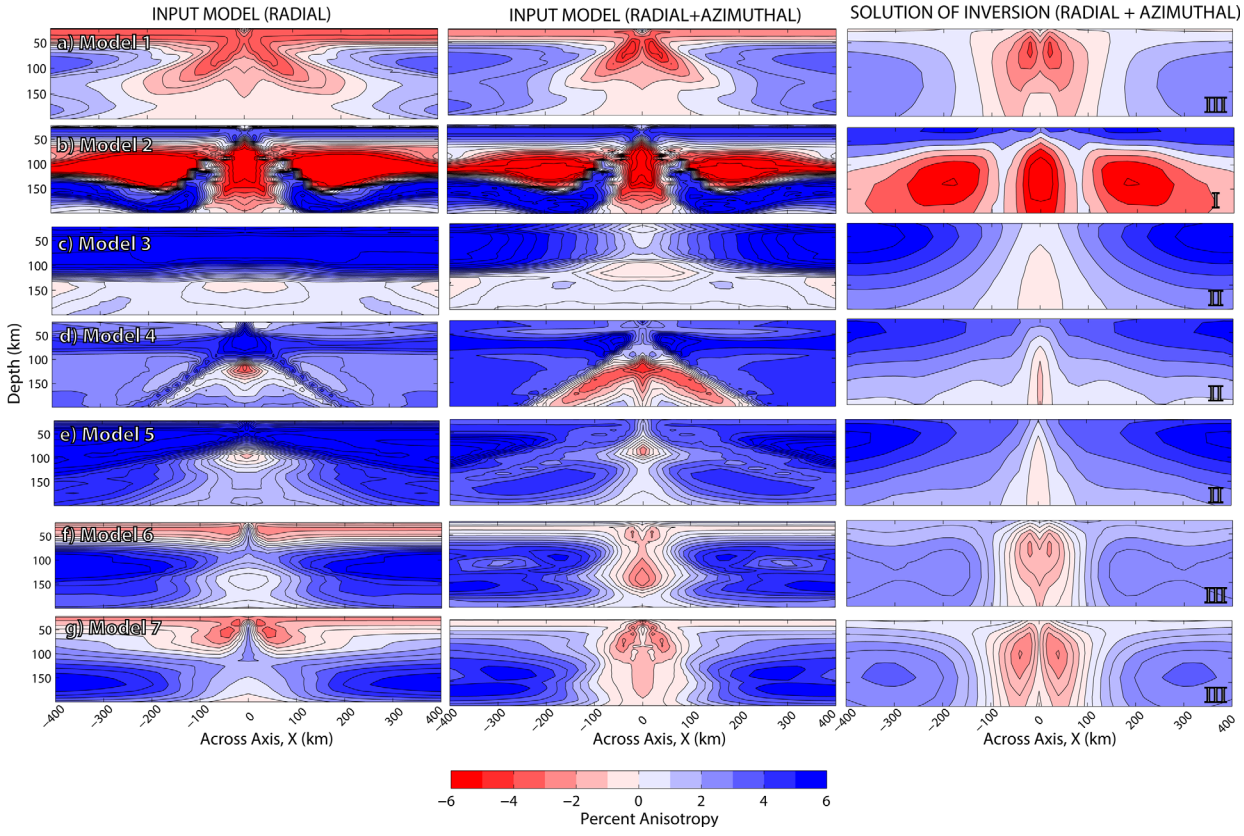

Figure 8. (left column) Percent radial anisotropy ($100 \times [Vsh - Vsv]/[(Vsh + Vsv)/2]$), of the input models in Figure 6 averaged parallel to the ridge axis, without the effects of azimuthal anisotropy. (middle column) same as the left column but including azimuthal terms for waves propagating perpendicular to the shown planes. (right column) Solutions of joint inversions of synthetic Rayleigh and Love wave phase velocities with the effects of both radial and azimuthal anisotropy. Figures 8a–8g are in the same order as for Figure 6.

and then flows roughly horizontally beneath the two plates (Figure 6a). Where the mantle turns the corner, the deformation is predicted to preferentially align the olivine *a* axes with a diagonal (in the vertical plane) orientation, slanting up and toward the ridge axis [*Blackman et al.*, 1996]. This results in negative anisotropy in two lobes extending downward and away from the ridge axis (to a depth of ~150 km at a distance of ~150 km from the ridge axis) where this shearing is active, as well as in a horizontal layer at depths 10–50 km across the whole model domain, where the diagonal fabric has been frozen into the lithosphere and transported off axis (Figure 6b). Figure 7a (left) shows the *Vsv* pattern determined by direct computation (section 2.5) and Figure 7a (right) shows *Vsv* determined via seismic inversion of synthetic phase velocities (section 2.3) derived from this model. The two images have similar structures. The low-velocity "asthenosphere" in these images thins at the ridge axis. This is a consequence of plotting *Vsv* instead of true isotropic velocity: the change in anisotropy from the off axis regions to on axis regions produces a corresponding change in *Vsv*. A similar effect is present in other models that will be discussed below.

[21] The apparent radial anisotropy obtained via direct computation is shown in Figure 8a (left); the apparent radial plus azimuthal anisotropy is shown in the middle figure; and the equivalent result from seismic inversion is shown in the right figure. The inversions recover a more diffuse form of the two lobes of negative anisotropy that are present on either side of the ridge axis.

[22] Model 2 simulates 2-D, active upwelling beneath a mid-ocean ridge due to melt retained in the mantle beneath the ridge axis (Figure 6b). In this model, porosity was computed based on calculations of melting rate, vertical Darcy flow, and conservation of melt mass [e.g., *Jha et al.*, 1994]. The buoyancy of the melt forms a pattern of rapid upwelling, focused in a ~150 km wide zone beneath the ridge axis, and flanked by downwellings of comparable width on both sides of the ridge axis [*Blackman et al.*, 1996; *Gaherty*, 2001].

The associated LPO creates a relatively complex pattern of *Vsv* (Figure 7b, left) and anisotropy (Figure 8b, left and middle). The inversion for *Vsv* recovers a body of low *Vsv* (<4.1 km/s) (Figure 7b, right) just beneath the ridge axis above the most rapid, buoyant upwelling, but does not recover much of the input structure below ~100 km. High-amplitude negative anisotropy (~−5%) is recovered in a ~175 km wide zone beneath the ridge axis as well as in two, ~250 km wide zones centered ~200 km away from the ridge axis (Figure 8b, right). Each of these regions tends to be overly smoothed relative to the input structure (Figure 8b, middle) in the vertical direction. Across the upper 100 km of the model, the positive anisotropy (blue region) seen in the input model is recovered by the inversion.

[23] In both Models 1 and 2, azimuthal anisotropy makes little difference to the apparent radial anisotropy of the input model as the *a* axes are only aligned perpendicular to and nowhere parallel to the direction of wave propagation (Figures 8a and 8b, left versus middle). The main effect occurs in the shallowest ~50 km (Model 1) to ~75 km (Model 2), where the *a* axes are largely horizontal and perpendicular to wave propagation, which leads to more positive apparent radial anisotropy.

4.2. Model 3: Purely Axisymmetric Flow of a Plume Beneath a Stationary Plate

[24] The gravitational self spreading of buoyant plume material is one possible driving force for delivering plume material along mid-ocean ridges [*Ribe et al*., 1995]. To examine an idealized situation of purely axisymmetric spreading, we consider a 3-D model of a plume rising beneath a stationary plate. Plume material rises from the base of the model in a vertical stem and then spreads radially from the stem along the base of the lithosphere (Figure 6c). When the seismic structure is time-averaged along the direction of wave propagation (again to simulate the situation of *Delorey et al*.'s [2007] study), the resulting *Vsv* model (obtained via direct computation) is symmetric but not laterally homogeneous (Figure 7c, left), with a "hot plume layer" or seismic low-velocity layer from ~40–120 km depth. The inversion of the synthetic surface wave phase velocities results in a similar image (Figure 7c, right).

[25] Relevant to anisotropy, the radially spreading plume produces an axisymmetric pattern of LPO in which the *a* axes preferentially align parallel to the flow where the radial shear is dominant (e.g., >~300 km radial distance from the plume center, at a depth of 100 km, Figure 6c), and perpendicular to the flow where the circumferential stretching of the spreading plume material is more important [*Fu et al*., 2012] (<300 km from the plume center, at a depth of 100 km, Figure 6c). When averaged along the direction of wave propagation, the apparent radial anisotropy of the input models (Figure 8, left and middle) is positive within the 100 km thick lithosphere and weak in the spreading plume material at depths of 100–200 km. The radial anisotropy image obtained by phase-velocity inversion (Figure 8c, right column) has a much smoother overall appearance, with low-amplitude negative values (<1%) in a ~80 km wide zone at depths >~75 km at the center of the image and positive values (>6%) in the shallowest 150 km at distances >150 km from the center of the image.

4.3. Model 4: Artificially Slow Spreading and Unidirectional Plume Flow along the Ridge Axis

[26] Another end-member concept of plume-ridge interaction involves a nearly unidirectional flow of the plume in a lithospheric "pipe" or channel along the ridge axis [*Vogt*, 1976]. This type of flow is promoted by very low-viscosity plumes and lithosphere that thickens rapidly away from the ridge axis [*Albers and Christensen*, 2001]. Model 4 simulates a "deep" lithospheric channel by imposing an artificially slow spreading rate (1 km/Myr, Table 1, Figure 6d). Images of *Vsv*, computed either directly (Figure 7d, left) or via phase-velocity inversion (Figure 7d, right), exhibit a corresponding low-velocity "channel" beneath the ridge axis due to this hot material. Inversions recover *Vsv* values of <4.2 km/s, in a channel that is ~240 km wide and ~130 km thick.

[27] In this model, the LPO that develops directly beneath the ridge axis is such that the *a* axes are primarily vertical at a depth of ~100 km, because this is near where the *Y-Z* shear is near zero and is changing sign. Hence the along-axis-average radial anisotropy is negative in a small zone at about 100 km depth (Figure 8d, left). Above and below this depth, the *a* axes are oriented with a large component being parallel to the ridge axis [*Fu et al*., 2012]. Without azimuthal effects, the average radial anisotropy is positive above and below 100 km directly beneath the ridge; with azimuthal effects, the apparent radial anisotropy is negative over a greater depth range (Figure 8d, middle versus left). For similar reasons, azimuthal anisotropy

increases the area of apparent negative anisotropy on the sides of the ridge axis. These results demonstrate an example of a situation in which *a* axes directed parallel to wave propagation create more negative apparent radial anisotropy as shown in the 1-D models. The inversions recover negative anisotropy ($<-1\%$) in a narrow ($\sim$50 km wide) column directly beneath the ridge axis at depths $>$75 km and do not resolve the input thin, sloping regions of negative anisotropy to the sides of the ridge at depths $>\sim$125 km. The inversions successfully recover the positive anisotropy in the shallowest 100 km to the sides of the ridge axis.

4.4. Model 5: Realistic Spreading Rate and Plume with Low Viscosity

[28] Model 5 (Figure 6e) is more realistic in that it simulates a plume with excess temperature (200°C) and radius (65 km), consistent with body wave tomography results [*Wolfe et al*., 1997; *Allen et al*., 2002; *Hung et al*., 2004], and the Reykjanes Ridge half spreading rate of 10 km/Myr. Here, the plume viscosity is relatively low owing to a temperature-dependent and pressure-dependent viscosity (see Table 1). The model predicts material to flow away from the plume stem both along and perpendicular to the ridge axis, such that a hot and seismically low-velocity region (Figure 7e, left) spreads out beneath the lithosphere, deepening as the thermal lithosphere thickens away from the ridge axis. The inversion for *Vsv* structure recovers similar structure (Figure 7e, right), but with a lower amplitude total variation.

[29] In this model, the pattern of LPO produced by along-axis flow directly beneath the ridge is crudely like that in Model 4, but the negative anisotropy in Model 5 is shallower primarily because it occurs beneath a thinner and more gradually thickening lithosphere (Figure 8e). Azimuthal anisotropy leads to more negative apparent radial anisotropy beneath the ridge axis, as was the case in Model 4. The anisotropy pattern recovered by the phase-velocity inversion shows a narrow ($\sim$50 km wide) zone of negative anisotropy beneath the ridge axis and high-amplitude ($\geq$4%) positive anisotropy in the upper 100–150 km of the model (Figure 8e, right).

4.5. Models 6 and 7: Realistic Spreading Rate and Plume with High Viscosity Due to Dehydration

[30] Models 6 and 7 (Figures 6f and 6g, respectively) are much like Model 5 except they include the dependence of viscosity on water content, which leads to relatively high viscosities above the anhydrous solidus [*Ito et al*., 1999]. Model 7 differs from Model 6 in simulating a hotter (300°C) and wider (150 km radius) plume, as well as having higher average viscosity in the whole model (Rayleigh number of 1×10^5 in Model 7 versus 1×10^6 in Model 6). In both models, the thicker, dehydrated lithosphere causes the buoyancy-driven spreading of the plume to be deeper ($>\sim$100 km in Model 6 and $>\sim$150 km in Model 7). The *Vsv* structures obtained via direct computation (Figures 7f and 7g, left) and obtained via phase-velocity inversion (Figures 7f and 7g, right) each show a layer of low velocities where the hot plume is present below the thermal lithosphere.

[31] For Model 6, at depths of 100–200 km beneath the ridge axis the plume flow is ridge parallel, causing the *a* axes of olivine to preferentially align subparallel to the ridge axis. Ignoring azimuthal anisotropy, the average radial anisotropy in this area is weakly positive at these depths (Figure 8f, left); including azimuthal anisotropy, the apparent anisotropy is negative (Figure 8f middle). A similar change to more negative anisotropy is found for Model 7 (Figure 8g). Shallower than $\sim$100 km, flow within the high viscosity, dehydrated layer is driven mainly by the seafloor spreading, and this forms a corner flow situation analogous to that in Model 1 without a plume. Like in Model 1, the corner flow in Models 6 and 7 creates two lobes of negative anisotropy extending diagonally downward and away from the ridge axis. In the upper 50 km of the mantle, the main effect of azimuthal anisotropy is to reduce the amplitude of negative anisotropy to the sides of the ridge axis. At greater depths, and beneath the ridge, the effect of azimuthal anisotropy is to make the anisotropy negative over a $\sim$100 km wide region. The inversions (Figures 8f and 8g, right) recover two, vertically smeared, lobes of negative anisotropy adjacent to the ridge axis. Model 7 shows the two lobes being more separated and wider ($\sim$100 km) than in Model 6, because the high viscosity, dehydrated layer is thicker, and the plume is wider, therefore the corner flow extends both deeper and further from the ridge.

5. Discussion of 3-D Models

[32] The patterns of anisotropy produced by inverting the synthetic phase velocities (Figure 8, right column) can be classified into three

distinctive categories. Pattern I is predicted by Model 2 and is characterized by strong negative anisotropy in three zones and positive anisotropy only in the shallowest 100 km across the whole model. Model 2 is the test of *Gaherty* [2001] hypothesis (1) of melt-buoyancy-driven, active upwelling beneath the ridge axis and downwelling on the sides of the ridge axis. Pattern II is produced by models of low-viscosity plumes (Models 3, 4, 5) and is characterized by a single, relatively narrow ($<\sim$100 km) zone of negative anisotropy in the solutions obtained by inversion. These models test hypothesis (3) involving along-axis flow and the alignment of the olivine *a* axes subparallel to wave propagation. Pattern III (Models 1, 6, 7) is characterized by two lobes of negative anisotropy on the sides of the ridge axis, and weak or positive anisotropy elsewhere. This structure is created by 2-D, plate-driven corner flow, which occurs in Model 1, because there is no plume, and in Models 6 and 7, because dehydration leads to a shallow layer with high-viscosity where the buoyancy of the plume has little influence on the flow. These models test hypothesis (2), which states that vertically oriented olivine *a* axes created beneath the ridge are transported off axis. The test shows that the hypothesized negative radial anisotropy occurs only in the shallowest 30–50 km (Figures 8a, 8f, and 8g, left) and is diminished by azimuthal effects (Figures 8a, 8f, and 8g, middle column) to the point where it is barely evident in the inversion solutions (Figures 8a, 8f, and 8g, right column).

[33] None of the patterns provide satisfactory matches to the anisotropy observed near the RR [*Gaherty*, 2001; *Delorey et al*., 2007]. These tests, therefore, show that the original hypotheses for the origin of the structure near the RR involving LPO are insufficient explanations in their simplest forms. Pattern I, due to ridge-parallel convective rolls driven by melt-retention buoyancy, successfully produces the two negative anomalies on the sides of the RR; however, it also produces strongly negative anisotropy directly beneath the ridge axis, contrary to the weak positive anisotropy observed. While we have not directly included the effect of melt in the mantle on *Vsv*, we speculate that a model with significant melt retention would predict low isotropic *Vsv* in the upwelling mantle directly beneath the ridge, and higher *Vsv* within the melt-barren mantle downwellings to either side of the ridge. These effects would even further increase the lateral variability in *Vsv* compared to that predicted by LPO alone (Figure 7), and such short-wavelength structure is simply not evident (Figure 1). Thus, this mechanism is unlikely to be the primary cause for the seismic structure beneath the RR. Pattern II, which involves the strongest along-axis flow, is the most inconsistent with the observed anisotropy pattern. This pattern can lead to substantially negative anisotropy, but only very close to the ridge axis and not off axis where it is present near the RR. Pattern III, which involves basic corner flow, shows two lobes of negative anisotropy on the sides of the ridge axis that are somewhat characteristic of the observed pattern. A broad zone ($>\sim$200 km) where melt is present (again not simulated) could be contributing to the observed broad low-velocity zone (Figure 1), and in fact, would be needed to account for lower *Vsv* values directly beneath the ridge at depths 50–150 km, where the model predicts slightly higher *Vsv* (Figure 7).

[34] A weakness of Pattern III is that the predicted lobes of negative anisotropy are too close to the ridge axis: they are centered within only $\sim$50 km on both sides of the ridge axis, not $\sim$100 km to the sides of the RR as imaged by *Delorey et al*. [2007]. If this type of flow is the cause for the observed pattern, then the mantle beneath the RR must be turning the corner further away from the ridge axis than currently predicted. Another complication is that whereas corner flow—in some form or another—is probably present beneath all mid-ocean ridges, the RR is the only ridge, known to date, associated with such strongly negative anisotropy. Studies using short-period surface waves at other mid-ocean ridges, detect radial anisotropy in the shallow upper mantle that is very weak [*Kutowski et al*., 2008] or distinctly positive [*Nishimura and Forsyth*, 1989; *Gaherty and Dunn*, 2007; *Conley and Dunn*, 2011]. To date, the lack of conclusive evidence for a wide zone of negative radial anisotropy beneath a mid-ocean ridge (other than the Reykjanes Ridge) is a serious problem for LPO with olivine A-type fabric, developing in response to simple corner flow as being a major source of the seismic anisotropy. Both seismic investigations and geodynamic models will need to be refined in order to achieve a better agreement between the two.

[35] There are other factors, not investigated here, that could contribute to the anomalous anisotropy beneath the flanks of the Reykjanes Ridge. (i) The presence of water in the Iceland mantle can lead to different olivine fabrics than the A-type considered here [*Karato et al*., 2007]. If so, the different fabrics could lead to different relationships between mantle deformation and LPO than

currently modeled. (ii) The current models assume that LPO develops only above a fixed, arbitrarily chosen depth of 200 km, whereas this depth is likely to vary with position due to variations in mantle temperature and stress [e.g., *Conder*, 2007] related to the Icelandic mantle plume. (iii) The presence of melt in the mantle can lead to LPO directions that can deviate by as much as 90° from those modeled here due to differing partitioning of strain between weak, melt-rich channels and stiffer, more crystalline material [*Holtzman et al.*, 2003]. (iv) Aligned melt channels can themselves create seismic anisotropy and *Holtzman and Kendall* [2010] proposed that melt channels—not LPO—are the primary cause of the anisotropy near the RR. Their idea is that negative anisotropy is created by melt channels concentrating along the lithosphere-asthenosphere boundary (LAB), which dips steeply ($\geq \sim 45°$) on the sides of the RR. Future geodynamic modeling efforts are needed to investigate the conditions needed to produce such a steeply dipping LAB and whether the associated melt bands can produce the observed anisotropy. (v) The tectonic configuration and mantle flow has varied in time. For example, circa 20 Ma some event resulted in the appearance of the diachronous V-shape ridges near the RR as well as the transition from orthogonally spreading ridge segments, separated by transform faults, to the current configuration of an obliquely spreading, relatively straight ridge without transform faults [*Jones et al.*, 2002; *Merkur'ev et al.*, 2009]. This age corresponds with the onset of the anomalous anisotropy that now exists beneath the flanks of the ridge. Future efforts considering the above factors should be explored to better reconcile predictions with these and new observations.

6. Conclusions

[36] We have investigated the cause of the two lobes of negative radial anisotropy detected on the sides of the Reykjanes Ridge (RR) by previous seismic studies [*Gaherty*, 2001; *Delorey et al.*, 2007]. Anisotropy is attributed to LPO of olivine A-type fabric in simple models with 1-D, layered structures as well as 2-D and 3-D geodynamic models with mantle flow and LPO evolution. Synthetic phase velocities of Love and Rayleigh waves traveling parallel to the ridge axis were produced and then inverted to mimic the conditions of the prior seismic studies. Inversions of synthetic data produced from imposed 1-D, layered structure, show that azimuthal anisotropy in the mantle can heavily impact the apparent radial anisotropy recovered by inverting data from surface waves traveling in nearly one direction, as was the case in the seismic studies. In particular, inversions recover negative anisotropy of amplitudes comparable to that detected near the RR if olivine *a* axes are preferentially aligned not only vertically but also subhorizontally in the plane of wave propagation.

[37] Geodynamic models of mantle flow, combined with calculations of crystallographic fabric evolution and seismic anisotropy are used to test prior hypotheses for the origin of the anisotropy near the RR involving LPO, as well as various types of mantle flow associated with plume-ridge interaction. Inversions of synthetic phase velocities from models involving rapid along-axis flow of low-viscosity plumes in the shallowest (depth $\leq$ 100 km) upper mantle produce the least favorable matches to the observed anisotropy. Ridge-parallel convective rolls due to melt-retention buoyancy reproduces the negative lobes of anisotropy on the sides of the ridge axis, but is problematic in predicting strongly negative anisotropy beneath the ridge axis as well as large variations in *Vsv* (via melt concentration changes) that are both not seen. Models with a viscous upper mantle, due to the extraction of water from the plume via partial melting, produce lobes of negative anisotropy on the sides of the ridge due to the rapid bending of mantle streamlines in a plate-driven corner flow. For this mechanism to be the main cause of the observed anisotropy, the predicted effects of corner flow must be wider than predicted near the RR, but narrower or overprinted by other mechanism at other mid-ocean ridges where negative anisotropy has not been detected. None of the types of mantle flow associated with plume-ridge interaction tested here with LPO of olivine A-type fabric fully explain the observations in their pure form. Other factors must also be important.

Acknowledgments

[38] We thank Ulrich Faul for the computer codes to implement *Jackson and Faul* [2010]. Many thanks also to two anonymous reviewers and editor Thorsten Becker for their constructive and exceptionally timely reviews. This study was funded by grant NSF-EAR 08–55814. SOEST contribution 8950.

References

Albers, M., and U. R. Christensen (2001), Channeling of plume flow beneath mid-ocean ridges, *Earth Planet. Sci. Lett.*, *187*(1–2), 207–220.

Allen, R.M., et al. (2002), Imaging the mantle beneath Iceland using integrated seismological techniques, *J. Geophys. Res.*, *107*(B12), 2325, doi:10.1029/2001JB000595.

Anderson, D. L. (1961), Elastic wave propagation in layered anisotropic media, *J. Geophys. Res.*, *66*(9), 2953–2963.

Backus, G. E. (1965), Possible forms of seismic anisotropy of the uppermost mantle under oceans, *J. Geophys. Res.*, *70*(14), 3429–3439.

Ballmer, M. D., J. van Hunen, G. Ito, P. J. Tackley, and T. A. Bianco (2007), Non-hotspot volcano chains originating from small-scale sublithospheric convection, *Geophys. Res. Lett.*, *34*, doi:10.1029/2007GL031636.

Becker, T. W., S. Chevrot, V. Schulte-Pelkum, and D. K. Blackman (2006), Statistical properties of seismic anisotropy predicted by upper mantle geodynamic models, *J. Geophys. Res.*, *111*, B08309, doi:10.1029/2005JB004095.

Bianco, T. A., G. Ito, J. van Hunen, M. D. Ballmer, and J. J. Mahoney (2008), Geochemical variation at the Hawaiian hot spot caused by upper mantle dynamics and melting of a heterogeneous plume, *Geochem. Geophys. Geosyst.*, *9*(11), Q11003, doi:11010.11029/12008GC002111.

Bianco, T. A., G. Ito, J. van Hunen, M. D. Ballmer, J. J. Mahoney (2011) Geochemical variations at intraplate hot spots caused by viable melting of a veined mantle plume, Geochem. *Geophys. Geosys.*, *12*, (*7*), Q0AC13, doi:10.1029/20111GC003658.

Blackman, D. K., J. A. Orcutt, D. W. Forsyth, and J. M. Kendall (1993), Seismic anisotropy in the mantle beneath an oceanic spreading centre, *Nature*, *366*(6456), 675–677.

Blackman, D. K., J. M. Kendall, P. R. Dawson, H. R. Wenk, D. Boyce, and J. P. Morgan (1996), Teleseismic imaging of subaxial flow at mid-ocean ridges: Traveltime effects of anisotropic mineral texture in the mantle, *Geophys. J. Int.*, *127*(2), 415–426.

Conder, J. (2007), Dynamically driven mantle flow and shear wave splitting asymmetry across the EPR, MELT area, *Geophys. Res. Lett.*, *34*, L16301, doi:10.1029/2007GL030832.

Conley, M. M., and R. A. Dunn (2011), Seismic shear wave structure of the uppermost mantle beneath the Mohns Ridge, *Geochem. Geophys. Geosyst.*, *12*, Q0AK01, doi:10.1029/2011GC003792.

Delorey, A., R. Dunn, and J. Gaherty (2007), Surface wave tomography of the upper mantle beneath the Reykjanes Ridge with implications for ridge hot-spot interaction, *J. Geophys. Res.*, *112*, B08313, doi:10.1029/2006JB004785.

Dziewonski, A. M., and D. L. Anderson (1981), Preliminary reference Earth model, *Phys. Earth Planet. Inter.*, *25*(4), 297–356.

Forsyth, D. W., S. C. Webb, L. M. Dorman, and Y. Shen (1998), Phase velocities of Rayleigh waves in the MELT experiment on the East Pacific Rise, *Science*, *280*(5367), 1235–1238.

Fu, Y. V., A. Li, G. Ito, and S. Hung (2012) Waveform modeling of shear wave splitting from anisotropic models in Iceland, *Geochem. Geophys. Geosyst.*, *13*, Q1200, doi:10.1029/2012GC004369.

Gaherty, J. B. (2001), Seismic evidence for hotspot-induced buoyant flow beneath the Reykjanes Ridge, *Science*, *293*(5535), 1645–1647.

Gaherty, J. B., and R. A. Dunn (2007), Evaluating hot spot-ridge interaction in the Atlantic from regional-scale seismic observations, *Geochem. Geophys. Geosyst.*, *8*, Q05006, doi:10.1029/2006GC001533.

Hirth, G., and D. L. Kohlstedt (1996), Water in the oceanic upper mantle: Implications for rheology, melt extraction and the evolution of the lithosphere, *Earth. Planet. Sci. Lett.*, *144*(1–2), 93–108.

Hirth, G., and D. L. Kohlstaedt (2003), Rheology of the upper mantle and the mantle wedge: A view from the experimentalists, in *Inside the Subduction Factory*, edited by J. Eiler, pp. 83–105, Geophys. Monogr. Ser., AGU, Washington, D. C.

Holtzman, B. K., and J.-M. Kendall (2010), Organized melt, seismic anisotropy, and plate boundary lubrication, *Geochem. Geophys. Geosyst.*, *11*, Q0AB06, doi:10.1029/2010GC003296.

Holtzman, B. K., D. L. Kohlstedt, M. E. Zimmerman, F. Heidelbach, T. Hiraga, and J. Hustof (2003), Melt segregation and strain partitioning: Implications for seismic anisotropy and mantle flow, *Science*, *301*, 1227–1230.

Hung, S., Y. Shen, and L. Chiao (2004), Imaging seismic velocity structure beneath the Iceland hot spot: A finite frequency approach, *J. Geophys. Res.*, *109*, B08305, doi:10.1029/2003JB002889.

Ito, G., J. Lin, and C. W. Gable (1996), Dynamics of mantle flow and melting at a ridge-centered hotspot: Iceland and the mid-Atlantic Ridge, *Earth Planet. Sci. Lett.*, *144*(1–2), 53–74.

Ito, G., Y. Shen, G. Hirth, and C. J. Wolfe (1999), Mantle flow, melting, and dehydration of the Iceland mantle plume, *Earth Planet. Sci. Lett.*, *165*(1), 81–96.

Jackson, I., and U. H. Faul (2010), Grainsize-sensitive viscoelastic relaxation in olivine: Towards a robust laboratory-based model for seismological application, *Phys. Earth Planet. Inter.*, *183*, 151–163.

Jha, K., E. M. Parmentier, and J. Phipps Morgan (1994), The role of mantledepletion and melt retention in spreading center segmentation, *Earth Planet. Sci. Lett*., *125*, 221–234.

Jones, S. M., N. White, and J. Mclennan (2002), V-shaped ridges around Iceland: Implications for spatial and temporal patterns of mantle convection, *Geochem. Geophys. Geosyst.*, *3*(10), 1059, doi:10.1029/2002GC000361.

Kaminski, E., N. M. Ribe, and J. T. Browaeys (2004), D-Rex, a program for calculation of seismic anisotropy due to crystal lattice preferred orientation in the convective upper mantle, *Geophys. J. Int.*, *158*(2), 744–752.

Karato, S.-I., H. Jung, I. Katayama, and P. Skemer (2007), Geodynamic significance of seismic anisotropy of the upper mantle: New insights from laboratory studies, *Annu. Rev. Earth Planet. Sci.*, *36*(1), 59–95.

Kutowski, B., G. Ekström, and A. M. Dziewoński (2008), Anisotropic shear-wave velocity structure of the Earth's mantle: A global model, *J. Geophys. Res.*, *113*, B06306, doi:10.1029/2007JB005169.

Li, A., and R. S. Detrick (2003), Azimuthal anisotropy and phase velocity beneath Iceland: Implication for plume-ridge interaction, *Earth Planet. Sci. Lett.*, *214*, 153–165.

Merkur'ev, S. A., C. DeMets, and N. I. Gurevich (2009), Geodynamic evolution of crustal accretion at the axis of the Reykjanes Ridge, Atlantic Ocean, *Geotectonics*, *43*(3), 194–207.

Montagner, J. P., and H. C. Nataf (1986), A simple method for inverting the azimuthal anisotropy of surface waves, *J. Geophys. Res.*, *91*(B1), 511–520.

Moresi, L., and M. Gurnis (1996), Constraints on the lateral strength of slabs from three-dimensional dynamic flow models, *Earth Planet. Sci. Lett.*, *138*(1–4), 15–28.

Nishimura, C. E., and D. W. Forsyth (1989), The anisotropic structure of the upper mantle in the Pacific, *Geophys. J. Int.*, *96*(2), 203–229.

Nowacki, A., J. M. Kendall, and J. Wookey (2012), Mantle anisotropy beneath the Earth's mid-ocean ridges, *Earth Planet. Sci. Lett.*, *317–318*, 56–67.

Pilidou, S., K. Priestley, E. Debayle, and Ó. Gudmundsson (2005), Rayleigh wave tomography in the North Atlantic: High resolution images of the Iceland, Azores and Eifel mantle plumes, *Lithos*, *79*(3–4), 453–474.

Ribe, N. M., U. R. Christensen, and J. Theißing (1995), The dynamics of plume-ridge interaction, 1: Ridge-centered plumes, *Earth Planet. Sci. Lett.*, *134*(1–2), 155–168.

Ruedas, T., H. Schmeling, G. Marquart, A. Kreutzmann, and A. Junge (2004), Temperature and melting of a ridge-centred plume with application to Iceland; Part I, dynamics and crust production, *Geophys. J. Int.*, *158*, 729–743.

Shimamura, H., T. Asada, K. Suyehiro, T. Yamada, and H. Inatani (1983), Longshot experiments to study velocity anisotropy in the oceanic lithosphere of the northwestern Pacific, *Phys. Earth Planet. Inter.*, *31*(4), 348–362.

Silver, P. G. (1996), Seismic anisotropy beneath the continents: Probing the depths of geology, *Annu. Rev. Earth Planet. Sci.*, *24*, 385–432.

Smith, M. L., and F. A. Dahlen (1973), Azimuthal dependence of Love and Rayleigh-wave propagation in a slightly anisotropic, *J. Geophys. Res.*, *78*(17), 3321–3333.

Takeuchi, H., and M. Saito. (1972), Seismic surface waves, in *Methods in Computational Physics*, vol. 11, edited by B.A. Bolt, Acad. Press, New York.

Tryggvason, K., E. S. Husebye, and R. Stefánsson (1983), Seismic image of the hypothesized Icelandic hot spot, *Tectonophysics*, *100*(1–3), 97–118.

Turcotte, D. L., and G. Schubert (1982), *Geodynamics: Applicationsof Continuum Physics to Geological Problems*, 450 pp., Wiley, New York.

Wolfe, C. J., and S. C. Solomon (1998), Shear-wave splitting and implications for mantle flow beneath the MELT region of the East Pacific Rise, *Science*, *280*(5367), 1230–1232.

Wolfe, C. J., I. Th. Bjarnason, J. C. VanDecar, and S. C. Solomon (1997), Seismic structure of the Iceland mantle plume, *Nature*, *385*(6613), 245–247.

Zhong, S., M. T. Zuber, L. Moresi, and M. Gurnis (2000), Role of temperature-dependent viscosity and surface plates in spherical shell models of mantle convection, *J. Geophys. Res.*, *105*(B5), 11,063–11,082.